*Research article*

# A comparative study for fractional simulations of Casson nanofluid flow with sinusoidal and slipping boundary conditions via a fractional approach

**Ali Raza[1], Umair Khan[2,3], Aurang Zaib[4], Wajaree Weera[5,*] and Ahmed M. Galal[6,7]**

[1] Department of Mathematics, University of Engineering and Technology, Lahore 54890, Pakistan
[2] Department of Mathematical Sciences, Faculty of Science and Technology, Universiti Kebangsaan Malaysia, UKM Bangi 43600, Selangor, Malaysia
[3] Department of Mathematics and Social Sciences, Sukkur IBA University, Sukkur 65200, Sindh Pakistan
[4] Department of Mathematical Sciences, Federal Urdu University of Arts, Science & Technology, Gulshan-e-Iqbal Karachi-75300, Pakistan
[5] Department of Mathematics, Faculty of Science, Khon Kaen University, Khon Kaen 40002, Thailand
[6] Department of Mechanical Engineering, College of Engineering in Wadi Alddawasir, Prince Sattam bin Abdulaziz University, Saudi Arabia
[7] Production Engineering and Mechanical Design Department, Faculty of Engineering, Mansoura University, P.O 35516, Mansoura, Egypt

**\* Correspondence:** Email: wajawe@kku.ac.th.

**Abstract:** This paper addresses a mixed and free convective Casson nanofluid flowing on an oscillating inclined poured plate with sinusoidal heat transfers and slip boundaries. As base fluid water is supposed and the suspension of nanofluid is formulated with the combination of individual copper $(Cu)$, titanium dioxide $(TiO_2)$ and aluminum oxide $(Al_2O_3)$ as nanoparticles, the dimensionless governing equations are generalized based on Atangana-Baleanu (AB) and Caputo-Fabrizio (CF) fractional operators for developing a fractional form. Then, for the semi-analytical solution of the momentum and thermal profiles, the Laplace transformation is utilized. To discuss the influences of various pertinent parameters on governing equations, graphical tablecomparison of the Nusselt number and skin friction is also inspected at different times and

numerical schemes. As a result, it has been concluded that both the momentum and energy profiles represent the more significant results for the AB-fractional model as related to the CF-fractional model solution. Furthermore, water-based titanium dioxide $(TiO_2)$ has a more progressive impact on the momentum as well as the thermal fields as compared to copper $(Cu)$ and aluminum oxide $(Al_2O_3)$ nanoparticles. The Casson fluid parameter represents the dual behavior for the momentum profile, initially momentum field decreases due to the Casson parameter but it then reverses its impact and the fluid flow moves more progressively.

## 1. Introduction

It is very tough to visualize humans living in a recent time without heat transference. Maximum heat transmission processes in heat systems are achieved by employing the thermal transmission of fluids. The utilization of conventional thermal transfer fluids like ethylene glycol, water, engine oil and methanol is finite because of their short heat conductions [1]. For the advancement of the energy effectiveness of systems in different fields of science and engineering, the conventional thermal transference of fluids was substituted by nanofluids (NFs) [2]. NFs are an emulsion of little complex non-metallic or metallic elements, named nanoparticles in the base as mentioned for earlier liquids [3]. Through the more significant heat conduction of nanoparticles, the use of NFs boosts the thermal transmission. The NFs, in terms of their thermal performance, construction, solidity, and properties, were studied by Aydin and Guru [4]. Although NFs are formed through scattering one kind of nanoparticles in the base liquid, the thermal characteristics of NFs might be enhanced by using hybrid nanofluids (HNFs). HNFs combine two or more two different nanoparticles in the base liquid. Suitable nanoparticle kinds with precise weight percent are utilized to attain the required thermal exchange percentage. The HNFs institute enormous utilization in various features of the human life cycle, for instance, in defense, microfluidics and transportation [5,6], in this mode, the idea of HNFs has been the topic of several numerical and experimental investigations. An excellent analysis of HNFs, their techniques of preparation and the features affecting their performance and areas of employment were examined in [7]. The water-based HNF of silicon dioxide and graphite was groomed by Dalkılıç et al. [8], and its thickness in dissimilar NP volume fractions and temperatures was calculated. The thickness increases by the volume fraction rise and temperature decline were established; the maximum thickness increase was also attained. Numerous researches work on the movement of HNFs have been investigated in the relevant literature; see [9,10]. A Casson fluid is an essential form of non-Newtonian fluid that acts identical to a flexible solid in which no movement happens with minor yield stress [11]. It is appropriate for cooling and heating operations because of its powerful influence on the energy communication rate, which qualifies it for application in numerous fields like diet processing, drilling, metallurgy, and biotechnology developments. A Casson fluid is helpful during the construction of printing ink [12]. Casson fluid is also proficiently efficient at describing many polymers' movement features extensively [13].

Moreover, experiments based on blood have established that blood can perform as a Casson fluid [14,15]. Human blood, tomato sauce, custard, toothpaste, foams, starch suspensions, yogurt, nail

polish and molten cosmetics are well-known examples of this fluid. Recently, Mustafa et al. [16] testified, when the speed is reducing and temperature is growing, raising the Casson parameter increases shear stress as well as thermal transfer. Mukhopadhyay et al. [17] exploited the shooting technique to study the flow of a Casson liquid as well as energy communication. Khalid et al. [18] studied the magneto-natural convection flow of a Casson fluid on a plate in a porous medium. Animasaun et al. [19] verified that the development in the Casson constraint source estimations enhances curve growth and reduces temperature curves. The influence of chemical reactions with a Casson liquid and a sphere was reviewed in [20]. Makinde et al. [21] discussed a meaningful connection between the influence of the Lorentz force and the movement of Casson fluid. The influence and skill of HNFs as the heat transfer fluid with a moving surface were numerically examined in [22]. A numerical investigation was done to study the HNFs boundary layer flow by Khashi'ie et al. [23]. They proved that the surface of a flat plate reduces the difference of the boundary layer and improves the heat transmission phenomena. The numerical solution and stability investigation for HNFs flow on a porous stretching/shrinking cylinder was discussed in [24] by utilizing the bvp4c problem solver in the Matlab package. They proved that a rise in the melting factor decreases the quantity of heat transmission and boosts the difference in the boundary layer. Ahmad et al. [25] investigated the analytical solution of a Casson NF flowing on an infinite vertical plate by utilizing the Caputo fractional derivatives definition.

The construction of different physical phenomena consequences complicated partial differential equations. The solution to such problems is relatively substantial in evaluating diverse types of physical phenomena. Fractional calculus excellently defines different approaches for investigating this type of problem. The terms, with the local and non-local kernels, are proficiently conserved by fractional technique. In the branch of fractional calculus, Caputo-Fabrizio (CF) and Atangana-Baleanu (AB) approaches are well-known techniques which have been extensively applied by investigators for several years in the past [26,27]. A well-known Indian mathematician, Tialk Raj Prabhakar, anticipated an innovative fractional operator along with three parameters. The Prabhakar fractional operator is a Mittag-Leffler function with three dissimilar fractional derivative operators. This operator has Mittag-Leffer tails using classical kernels positively [28]. Ali et al. [29] applied a Laplace transform and fractional approach to discuss a viscous fractional fluid model. Raza et al. [30, 31] applied Prabhakar and Caputo fractional approach and a Laplace transform to study different fluid models and tools to improve the thermal transfer methods. Samia et al. [32] discussed a rate-type fractional model with a semi-analytical approach. Different numerical familiar techniques were applied for a fractional Oldroyd-B fluid mathematical model in [33]. Wang et al. [34] applied a Prabhakar approach to examine the blood-based HNF models with diverse nanoparticles by considering the Newtonian heating effect. Jie et al. [35] discussed the Brinkman NF fractional model and sinusoidal oscillations and submitted significant results. Suganya et al. [36] discussed an innovative numerical technique for 2-D stimulation energy along with an unsteady and revolving HNF flow for stretching and moving surfaces by exploiting the explicit finite-difference method. Their results revealed that the stimulation energy controls the thermal transmission amount. Abu Bakar et al. [37]studied the flow of HNFs over a porous medium along with the slip and radiation effects on a shrinking sheet by employing the shooting method. They perceived the rise of thermal transfer in the HNF relative to the usual NF. Shoeibi et al. [38] studied the glass chilling of a double-slope lunar still by utilizing an HNF ($TiO_2$-$Al_2O_3$) at a 0.4% concentration numerically. Kanti et al. [39] applied the two-step technique to formulate the nanofluids. Their results exposed that the thermal conductivity of the NFs increased with increasing concentration and temperature. Nadeem et al. [40] discussed the heat transmission and MHD (magnetohydrodynamics) second-grade stagnation point flow of HNF

with a convectively heated porous sheet to enhance the quantity of heat transfer by exploiting the numerical bvp4c method.

After reviewing the above literature, we have examined the Casson NF with sinusoidal heat transference and slip boundaries in this article. Different nanoparticles, i.e., copper $(Cu)$, titanium dioxide $(TiO_2)$ and aluminum oxide $(Al_2O_3)$ have been utilized for the suspension of NFs with water as the base fluid. The comparative analysis of the attained results of governed equations with innovative fractional derivatives, i.e., AB and CF-time fractional derivatives are examined. The semi-analytical solution of thermal and momentum fields is attained with the assistance of the Laplace transform and some numerical methods. To analyze the effects of different parameters on the governing equations, graphical and numerical comparisons are discussed with different values of parameters. Furthermore, the numerical comparison of the Nusselt number and skin friction is inspected at different times and numerical schemes.

## 2. Problem description

In this manuscript, we have supposed a free mixed-convection viscous Casson NF flowing on an oscillating poured inclined plate due to the influence of applied inclined magnetic field with a strength of $B_o$ . The flowing Casson fluid is mixed with different $(Al_2O_3, Cu, TiO_2)$ nanoparticles. Thermophysical properties and their values of base fluid and nanoparticles are described in Tables 1 and 2. Primarily at $t = 0$, the temperature and inclined poured plate are both in a stable position. With the time at $t > 0^+$, the inclined plate begins to vibrate with a velocity $U_o Cos(\omega t)$, where $\omega$ shows the frequency of oscillations of the inclined plate. Due to the plate oscillations and rise in the thermal profile, the fluid also begins to flow on the oscillating plate with the same velocity as the plate oscillations, as displayed in Figure 1.

**Table 1.** Model for thermophysical properties of NF quantities.

| Thermal features | Regular NF |
|---|---|
| Density | $\rho_f = \dfrac{\rho_{nf}}{(1-\varphi) + \varphi \frac{\rho_s}{\rho_s}}$ |
| Dynamic Viscosity | $\mu_f = \mu_{nf}(1-\varphi)^{2.5}$ |
| Electrical conductivity | $\sigma_f = \dfrac{\sigma_{nf}}{\left(1 + \dfrac{3\left(\frac{\sigma_s}{\sigma_f}-1\right)\varphi}{\left(\frac{\sigma_s}{\sigma_f}+2\right)-\left(\frac{\sigma_s}{\sigma_f}-1\right)\varphi}\right)}$ |
| Thermal conductivity | $k_f = \dfrac{k_{nf}}{\left(\frac{k_s+(n-1)k_f-(n-1)(k_f-k_s)\varphi}{k_s+(n-1)k_f+(k_f-k_s)\varphi}\right)}$ |
| Heat capacitance | $(\rho C_p)_f = \dfrac{(\rho C_p)_{nf}}{(1-\varphi) + \varphi \frac{(\rho C_p)_s}{(\rho C_p)_f}}$ |
| Thermal Expansion Coefficient | $(\rho \beta)_f = \dfrac{(\rho \beta)_{nf}}{(1-\varphi) + \varphi \frac{(\rho \beta)_s}{(\rho \beta)_f}}$ |

**Table 2.** Thermal characteristics of base fluids and nanoparticles [45].

| Material | Water | Al$_2$O$_3$ | Cu | TiO$_2$ |
|---|---|---|---|---|
| $\rho(kg/m^3)$ | 997.1 | 3970 | 8933 | 4250 |
| $C_p(J/kgK)$ | 4179 | 765 | 385 | 686.2 |
| $k(W/mK)$ | 0.613 | 40 | 401 | 8.9528 |
| $\beta_T \times 10^5 (K^{-1})$ | 21 | 0.85 | 1.67 | 0.90 |
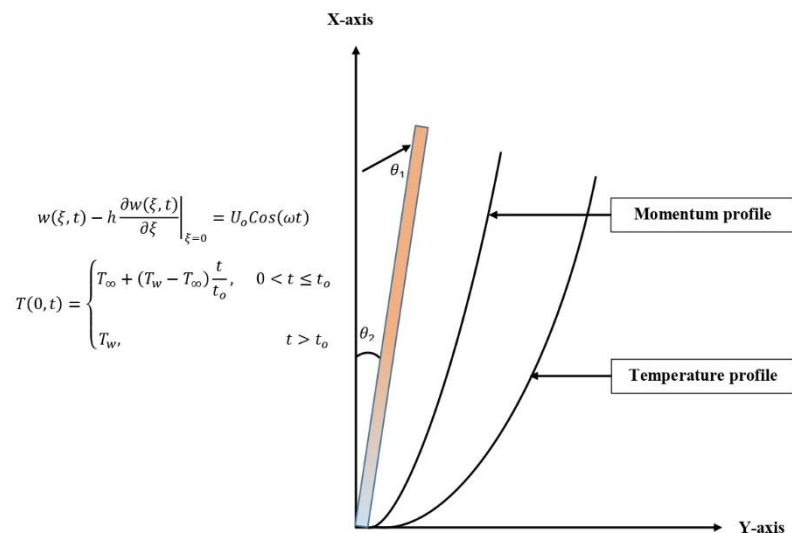


**Figure 1.** Geometry of the flow.

By neglecting the pressure gradient and utilizing the Boussinesq's [41,42] and Rosseland estimations, the governed equations for this fractional model can be originated as follows [43,44]:

$$\rho_{nf} \frac{\partial w(\xi,t)}{\partial t} = \mu_{nf}\left(1 + \frac{1}{\lambda_1^*}\right)\frac{\partial^2 w(\xi,t)}{\partial \xi^2} - \left(\sigma_{nf}B_o^2 Sin(\theta_1) + \frac{\mu_{nf}\varphi}{K}\right)w(\xi,t) + g(\rho\beta)_{nf}[T(\xi,t) - T_\infty]Cos(\theta_2),$$

(1)

$$\left(\rho C_p\right)_{nf}\frac{\partial T(\xi,t)}{\partial t} = k_{nf}\frac{\partial^2 T(\xi,t)}{\partial \xi^2},$$

(2)

with suitable conditions, as follows

$$w(\xi,0) = 0, T(\xi,0) = T_\infty; \ \xi > 0,$$

(3)

$$w(\xi,t) - h\frac{\partial w(\xi,t)}{\partial \xi}\bigg|_{\xi=0} = U_o Cos(\omega t), T(0,t) = \begin{cases} T_\infty + (T_w - T_\infty)\frac{t}{t_o}, 0 < t \le t_o, \\ \\ T_w, t > t_o, \end{cases}$$

(4)

$$w(\xi,t) \to 0, T(\xi,t) \to T_\infty; \ \xi \to \infty, t > 0.$$

(5)

Now, we introduce the appropriate non-dimensional parameters to non-dimensionalize the leading perspective conditions, Eqs (1) and (2):

$$w^* = \frac{w}{w_o}, \xi^* = \frac{\xi U_o}{v_f}, h^* = \frac{hU_o^2}{v} t^* = \frac{t}{t_o}, t_o = \frac{v_f}{U_o^2}, T^* = \frac{T-T_\infty}{T_w-T_\infty}.$$

By neglecting the star notation, the governing Eqs (1) and (2) and corresponding conditions in the non-dimensional form will become as

$$\Pi_1 \frac{\partial w(\xi,t)}{\partial t} = \Pi_2 \lambda_1 \frac{\partial^2 w(\xi,t)}{\partial \xi^2} - \left(\Pi_3 MSin(\theta_1) + \frac{\Pi_2}{K}\right) w(\xi,t) + \Pi_4 GrCos(\theta_2)T(\xi,t), \quad (6)$$

$$\Pi_5 Pr \frac{\partial T(\xi,t)}{\partial t} = \Pi_6 \frac{\partial^2 T(\xi,t)}{\partial \xi^2}, \quad (7)$$

with the non-dimensional conditions:

$$w(\xi,0) = 0, T(\xi,0) = 0; \xi > 0, \quad (8)$$

$$w(\xi,t) - h\frac{\partial w(\xi,t)}{\partial \xi}\bigg|_{\xi=0} = Cos(\omega t), T(0,t) = \begin{cases} t, 0 < t \le 1, \\ \\ 1, t > 1, \end{cases} \quad (9)$$

$$w(\xi,t) \to 0, T(\xi,t) \to 0; \xi \to \infty, t > 0. \quad (10)$$

In Eq (8) the initial conditions of the flowing mathematical model are described with the zero velocity and temperature at time $t = 0$. And in Eq (9) the boundary conditions at $\xi = 0$ are described with slipping boundary effect and sinusoidal thermal conditions, where

$$\Pi_1 = (1 - \varphi)\rho_f + \varphi\frac{\rho_s}{\rho_f}, \Pi_2 = \frac{1}{(1-\varphi)^{2.5}}, \Pi_3 = \frac{\sigma_{hnf}}{\sigma_f},$$

$$\Pi_4 = (1 - \varphi) + \varphi\frac{(\rho\beta_T)_s}{(\rho\beta_T)_f}, \Pi_5 = (1 - \varphi) + \varphi\frac{(\rho C_p)_s}{(\rho C_p)_f},$$

$$\Pi_6 = \frac{(1-\phi)+2\phi\frac{k_s}{k_s-k_f}ln\left(\frac{k_s-k_f}{2k_f}\right)}{(1-\phi)+2\phi\frac{k_s}{k_s-k_f}ln\left(\frac{k_s+k_f}{2k_f}\right)}, \lambda_1 = 1 + \frac{1}{\lambda_1^*}, Gr = \frac{g\beta_f(T_w-T_\infty)}{U_o^3},$$

$$Pr = \frac{\mu_f(C_p)_f}{k_f}, M = \frac{v_f\sigma_f B_o^2}{\rho_f U_o^2}, K = \frac{kU_o^2}{v_f\varphi}.$$

## 3. Some basic preliminaries

**Definition 1.** The mathematical form of the AB-fractional derivative for the function $u(y,t)$ is

$$^{AB}\mathfrak{D}_t^\beta u(y,t) = \frac{1}{1-\beta}\int_0^t E_\beta\left[\frac{\beta(t-z)^\beta}{1-\beta}\right]u'_{(y,t)}dt; \ 0 < \beta < 1, \quad (11)$$

where $^{AB}\mathfrak{D}_t^\beta$ is the AB-fractional operator with fractional order parameter $\beta$ [46] and $E_\beta(z)$ is a Mittag-Leffer function with the mathematical form of

$$E_\beta(z) = \sum_{r=0}^\infty \frac{z^\beta}{\Gamma(r\beta+1)}; \ z \in \mathbb{C}.$$

The Laplace transform of the AB-fractional derivative (Eq(5)) can be well-defined as [47]

$$\mathcal{L}\left\{^{AB}\mathfrak{D}_t^\beta w(\xi,t)\right\} = \frac{q^\beta \mathcal{L}[w(\xi,t)]-q^{\beta-1}w(\xi,0)}{(1-\beta)q^\beta+\beta}, \quad (12)$$

where $q$ is the transformed constraint via the Laplace scheme.

**Definition 2.** The CF-time-fractional derivative for the function $u(y,t)$ can be notarized as

$$^{CF}\mathfrak{D}_t^\alpha u(y,t) = \frac{1}{1-\alpha} \int_0^t exp\left(\frac{\alpha(1-\tau)}{1-\alpha}\right) u'(y,t)d\tau\,; \; 0 < \alpha < 1, \tag{13}$$

where $^{CF}\mathfrak{D}_t^\alpha$ is the CF-fractional operator with non-integer order $\alpha$, and its Laplace transformation is [48,49]

$$\mathcal{L}\left\{^{CF}\mathfrak{D}_t^\alpha w(\xi,t)\right\} = \frac{s\mathcal{L}[w(\xi,t)]-w(\xi,0)}{(1-\alpha)s+\alpha}. \tag{14}$$

## 4. AB-fractional model

The dimensionless version of the AB-fractional model may be attained by substituting the partial derivative with the AB-time fractional operator $^{AB}\mathfrak{D}_t^\beta$ of Eqs (6) and (7).

$$\Pi_1{}^{AB}\mathfrak{D}_t^\beta w(\xi,t) = \Pi_2\lambda_1\frac{\partial^2 w(\xi,t)}{\partial\xi^2} - \left(\Pi_3 MSin(\theta_1) + \frac{\Pi_2}{K}\right)w(\xi,t) + \Pi_4 GrCos(\theta_2)T(\xi,t), \tag{15}$$

$$\Pi_5 Pr\,^{AB}\mathfrak{D}_t^\beta T(\xi,t) = \Pi_6\frac{\partial^2 T(\xi,t)}{\partial\xi^2}, \tag{16}$$

where $^{AB}\mathfrak{D}_t^\beta$ signifies the AB-fractional operator.

### 4.1. Energy profile by AB

Using the Laplace transform to solve the energy equation (Eq (16)), we have

$$\Pi_5 Pr\left(\frac{q^\beta\mathcal{L}[T(\xi,t)]-q^{\beta-1}\bar{T}(\xi,0)}{(1-\beta)q^\beta+\beta}\right) = \Pi_6\frac{\partial^2\bar{T}(\xi,t)}{\partial\xi^2} \tag{17}$$

with the following transformed conditions:

$$\bar{T}(\xi,q) = \frac{1-e^{-q}}{q^2}, \text{ and } \bar{T}(\xi,q) \to 0 \text{ as } \xi \to \infty.$$

Exploiting the above transformed conditions, the simulation of the energy profile is summarized as

$$\bar{T}(\xi,q) = \frac{1-e^{-q}}{q^2}e^{-\xi\sqrt{\left(\frac{\Pi_5 Pr}{\Pi_6}\frac{q^\beta}{(1-\beta)q^\beta+\beta}\right)}}. \tag{18}$$

In Tables 3–5, we show the inverse results for Eq (18) that were obtained numerically by using inverse procedures such as the Stehfest and Tzou's approaches.

### 4.2. Momentum profile by AB

Applying the Laplace transform to Eq (15) and its accompanying conditions, we acquire the velocity solution as

$$\Pi_1 \left( \frac{q^\beta \mathcal{L}[w(\xi,t)] - q^{\beta-1}w(\xi,0)}{(1-\beta)q^\beta + \beta} \right) = \Pi_2\lambda_1 \frac{\partial^2 \overline{w}(\xi,q)}{\partial \xi^2} - \left( \Pi_3 MSin(\theta_1) + \frac{\Pi_2}{K} \right) \overline{w}(\xi,q)$$

$$+ \Pi_4 GrCos(\theta_2)\overline{T}(\xi,q) \tag{19}$$

with the transformed conditions:

$$\overline{w}(\xi,q) - h\frac{\partial \overline{w}(\xi,q)}{\partial \xi}\bigg|_{\xi=0} = \frac{\omega}{\omega^2+q^2} \text{ and } \overline{w}(\xi,q) \to 0 \text{ as } \xi \to \infty. \tag{20}$$

Utilizing conditions of Eq (20), the solution of Eq (19) will become

$$\overline{w}(\xi,q) = \frac{1}{1 + h\sqrt{\frac{1}{\Pi_2\lambda_1}\left(\Pi_3 MSin(\theta_1) + \frac{\Pi_2}{K} + \frac{\Pi_1 q^\beta}{(1-\beta)q^\beta+\beta}\right)}} \times$$

$$\left( \frac{\Pi_4 GrCos(\theta_2)}{\Pi_2\lambda_1} \frac{1-e^{-q}}{q^2} \frac{1 + h\sqrt{\frac{\Pi_5 Pr}{\Pi_6}\frac{q^\beta}{(1-\beta)q^\beta+\beta}}}{\left(\frac{\Pi_5 Pr}{\Pi_6}\frac{q^\beta}{(1-\beta)q^\beta+\beta}\right) - \frac{1}{\Pi_2\lambda_1}\left(\Pi_3 MSin(\theta_1) + \frac{\Pi_2}{K} + \frac{\Pi_1 q^\beta}{(1-\beta)q^\beta+\beta}\right)} + \frac{\omega}{\omega^2+q^2} \right) \times$$

$$e^{-\xi\sqrt{\frac{1}{\Pi_2\lambda_1}\left(\Pi_3 MSin(\theta_1)+\frac{\Pi_2}{K}+\frac{\Pi_1 q^\beta}{(1-\beta)q^\beta+\beta}\right)}} -$$

$$\frac{\Pi_4 GrCos(\theta_2)}{\Pi_2\lambda_1} \frac{1-e^{-q}}{q^2} \frac{e^{-\xi\sqrt{\frac{\Pi_5 Pr}{\Pi_6}\frac{q^\beta}{(1-\beta)q^\beta+\beta}}}}{\left(\frac{\Pi_5 Pr}{\Pi_6}\frac{q^\beta}{(1-\beta)q^\beta+\beta}\right) - \frac{1}{\Pi_2\lambda_1}\left(\Pi_3 MSin(\theta_1)+\frac{\Pi_2}{K}+\frac{\Pi_1 q^\beta}{(1-\beta)q^\beta+\beta}\right)}. \tag{21}$$

## 5. CF-fractional model

By substituting the partial derivative with respect to time with the CF-fractional operator $^{CF}\mathfrak{D}_t^\alpha$, the model equations for the CF-fractional derivative will be obtained as

$$\Pi_1 {}^{CF}\mathfrak{D}_t^\alpha w(\xi,t) = \Pi_2\lambda_1 \frac{\partial^2 w(\xi,t)}{\partial \xi^2} - \left( \Pi_3 MSin(\theta_1) + \frac{\Pi_2}{K} \right) w(\xi,t) + \Pi_4 GrCos(\theta_2)T(\xi,t), \tag{22}$$

$$\Pi_5 Pr {}^{CF}\mathfrak{D}_t^\alpha T(\xi,t) = \Pi_6 \frac{\partial^2 T(\xi,t)}{\partial \xi^2}, \tag{23}$$

where $^{CF}\mathfrak{D}_t^\alpha$ signifies the CF-fractional operator. With the following transformed conditions:

$$w(\xi,0) = 0, T(\xi,0) = 0; \ \xi > 0,$$

$$w(\xi,t) - h\frac{\partial w(\xi,t)}{\partial \xi}\bigg|_{\xi=0} = Cos(\omega t), T(0,t) = \begin{cases} t, 0 < t \le 1, \\ \\ 1, t > 1, \end{cases}$$

$$w(\xi,t) \to 0, T(\xi,t) \to 0; \ \xi \to \infty, t > 0.$$

### 5.1. Energy field by CF

Because the thermal profile in Eq (23) is agnostic of the momentum profile, applying the Laplace transform to the heat equation (Eq (23)) yields

$$\Pi_5 Pr\left(\frac{s\mathcal{L}[T(\xi,t)]-T(\xi,0)}{(1-\alpha)s+\alpha}\right) = \Pi_6 \frac{\partial^2 \bar{T}(\xi,s)}{\partial \xi^2}, \tag{24}$$

with the following conditions:

$$\bar{T}(\xi,s) = \frac{1-e^{-s}}{s^2} \text{ and } \bar{T}(\xi,s) \to 0 \text{ as } \xi \to \infty.$$

Employing the above conditions, the thermal profile will be

$$\bar{\vartheta}(y,s) = \frac{1-e^{-s}}{s^2} e^{-\xi\sqrt{\left(\frac{\Pi_5 Pr\ a_1 s}{\Pi_6\ s+a_2}\right)}}. \tag{25}$$

Again the Laplace inverse of the above equation can be observed numerically in Table 4.

## 5.2. Momentum field by CF

Now, for the velocity solution, apply the Laplace transform to the CF-fractional version given by Eq (22), as well as the temperature solution found in Eq (25)

$$\frac{\partial^2 \bar{w}(\xi,s)}{\partial \xi^2} - \frac{1}{\Pi_2 \lambda_1}\left(\Pi_3 MSin(\theta_1) + \frac{\Pi_2}{K} + \frac{\Pi_1 a_1 s}{s+a_2}\right)\bar{w}(\xi,s) = -\frac{\Pi_4 GrCos(\theta_2)}{\Pi_2 \lambda_1}\bar{T}(\xi,s), \tag{26}$$

with the following conditions:

$$\bar{w}(\xi,s) - h\frac{\partial \bar{w}(\xi,s)}{\partial \xi}\bigg|_{\xi=0} = \frac{\omega}{\omega^2+s^2} \text{ and } \bar{w}(\xi,s) \to 0 \text{ as } \xi \to \infty. \tag{27}$$

Using the condition mentioned earlier, the follow-up studies of Eq (26) may be obtained.

$$\bar{w}(\xi,s) = \frac{1}{1 + h\sqrt{\frac{1}{\Pi_2 \lambda_1}\left(\Pi_3 MSin(\theta_1) + \frac{\Pi_2}{K} + \frac{\Pi_1 a_1 s}{s+a_2}\right)}} \times$$

$$\left(\frac{\Pi_4 GrCos(\theta_2)}{\Pi_2 \lambda_1}\frac{1-e^{-q}}{q^2}\frac{1 + h\sqrt{\frac{\Pi_5 Pr\ a_1 s}{\Pi_6\ s+a_2}}}{\left(\frac{\Pi_5 Pr\ a_1 s}{\Pi_6\ s+a_2}\right) - \frac{1}{\Pi_2 \lambda_1}\left(\Pi_3 MSin(\theta_1) + \frac{\Pi_2}{K} + \frac{\Pi_1 a_1 s}{s+a_2}\right)} + \frac{\omega}{\omega^2+q^2}\right) \times$$

$$e^{-\xi\sqrt{\frac{1}{\Pi_2 \lambda_1}\left(\Pi_3 MSin(\theta_1)+\frac{\Pi_2}{K}+\frac{\Pi_1 a_1 s}{s+a_2}\right)}} - \frac{\Pi_4 GrCos(\theta_2)}{\Pi_2 \lambda_1}\frac{1-e^{-q}}{q^2}\frac{e^{-\xi\sqrt{\frac{\Pi_5 Pr\ a_1 s}{\Pi_6\ s+a_2}}}}{\left(\frac{\Pi_5 Pr\ a_1 s}{\Pi_6\ s+a_2}\right) - \frac{1}{\Pi_2 \lambda_1}\left(\Pi_3 MSin(\theta_1)+\frac{\Pi_2}{K}+\frac{\Pi_1 a_1 s}{s+a_2}\right)}. \tag{28}$$

We will utilize Stehfest and Tzou's numerical methods to compute the inverse Laplace transform of the temperature and velocity profiles using the AB and CF-fractional derivatives of Eqs (18), (21), (25) and (28), correspondingly [50–52]:

$$w(\xi,t) = \frac{ln(2)}{t}\sum_{n=1}^{M} v_n \bar{u}\left(\xi, n\frac{ln(2)}{t}\right),$$

$$v_n = (-1)^{n+\frac{M}{2}}\sum_{p=\frac{q+1}{2}}^{min\left(q,\frac{M}{2}\right)} \frac{p^{\frac{M}{2}}(2p)!}{\left(\frac{M}{2}-p\right)!p!\ (p-1)!\ (q-p)!\ (2p-q)!},$$

$$w(\xi,t) = \frac{e^{4.7}}{t}\left[\frac{1}{2}\bar{w}\left(r,\frac{4.7}{t}\right) + Re\left\{\sum_{j=1}^{N}(-1)^k \bar{w}\left(r,\frac{4.7+k\pi i}{t}\right)\right\}\right].$$

## 6. Results and discussion

The fundamental goal of this investigation was to demonstrate the importance of fractional derivatives for the Casson-type NF by means of AB and CF derivatives. For the energy and momentum equations, an NF mixed with various nanoparticles, such as $Al_2O_3$, $Cu$, $TiO_2$ was assumed and water was applied as the base fluid. The solution of the non-dimensional governing equations, i.e., the energy and momentum fields were found by applying the Laplace approach to the AB and CF-fractional models. The impacts of various constraints on non-dimensional governing equations are visually shown in Figures 2–13. The results of the numerical analysis of the Nusselt number and the skin friction are shown in Tables 3–5.

The effects of the fractional parameters $(\alpha, \beta)$ on temperature are shown in Figure 2(a) and 2(b). It is perceived that the temperature behavior decreases with growing estimations of fractional parameters for both fractional approaches. The AB-fractional operators have a more substantial impact than the CF-fractional operators on the energy profile. Such an impact happens because of the kernel of both diverse fractional operators. Figure 2(b) also shows the comparison of two different nanoparticles indicating that titanium dioxide ($TiO_2$)-based NFs have a relatively more progressive value than copper ($Cu$)-based NFs, due to the physical characteristics of the considered nanoparticles. Figure 3(a) and 3(b) were made to intercept the response of the temperature profile when the volume fraction of the $TiO_2$ and $Cu$ nanoparticles are equally varied. The response of the temperature field declined for improvement of the volume fraction ($\varphi$) for both fractional models. Figure 3(b) shows that the profile of the temperature of the $TiO_2$-based NF was better than that of the $Cu$-based NF. These suspension consequences are due to a growth in the thickness of the subsequent impact of the nanoparticles. Further, this effect is primarily attributed to the thermal features of the included nanoparticles, which refine the thermal presentation of the host fluid. Figure 4(a) and 4(b) were designed for the temperature profile to display the impacts of the $Pr$; the thermal boundary layer is shown as the same for both cases of fractional techniques. The temperature profile can be perceived as reciprocal performance for heat transmission over the whole domain. Figure 4(b) shows that the temperature for the normal working-based fluid. Here, the rising impacts of $Pr$ decelerates the temperature profile.
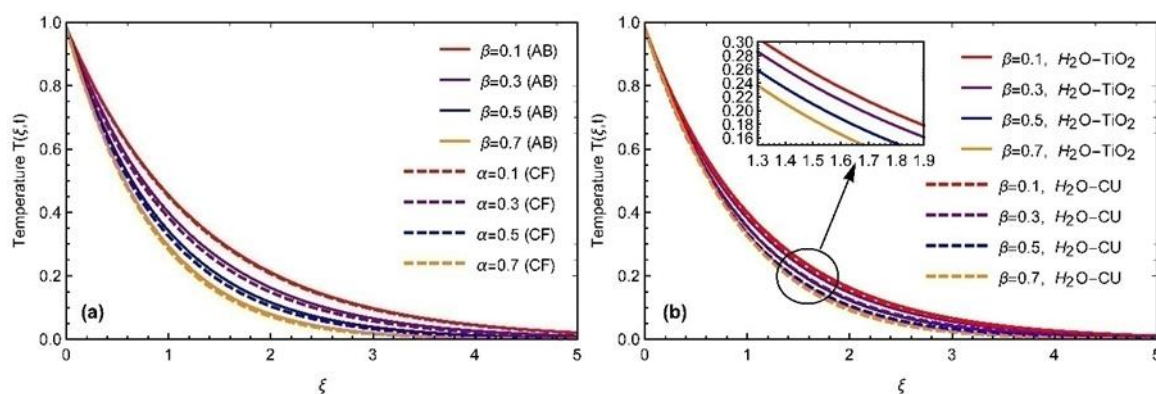


**Figure 2.** Temperature profile against $\xi$ due to $\alpha$, $\beta$ when $Pr = 6.2$, $\varphi = 0.02$, and $t = 1.0$.
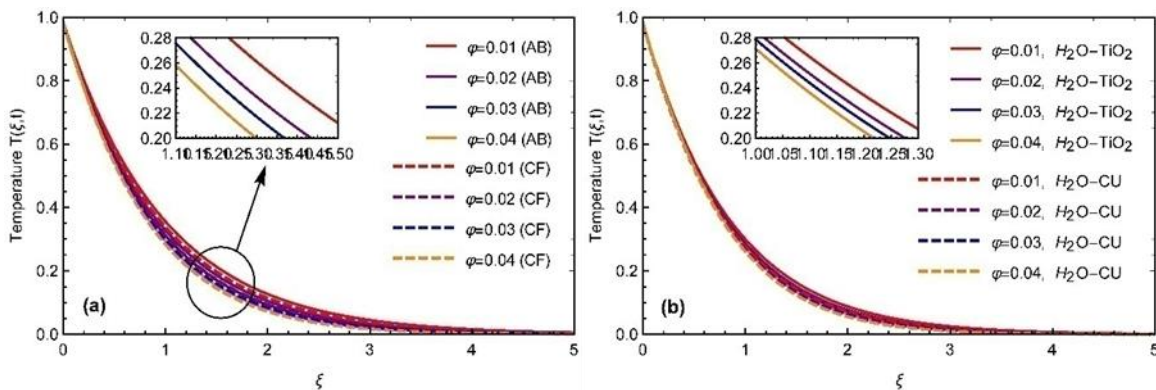
**Figure 3.** Temperature profile against $\xi$ due to $\varphi$ when $\alpha, \beta = 0.5, Pr = 6.2$, and $t = 1.0$.
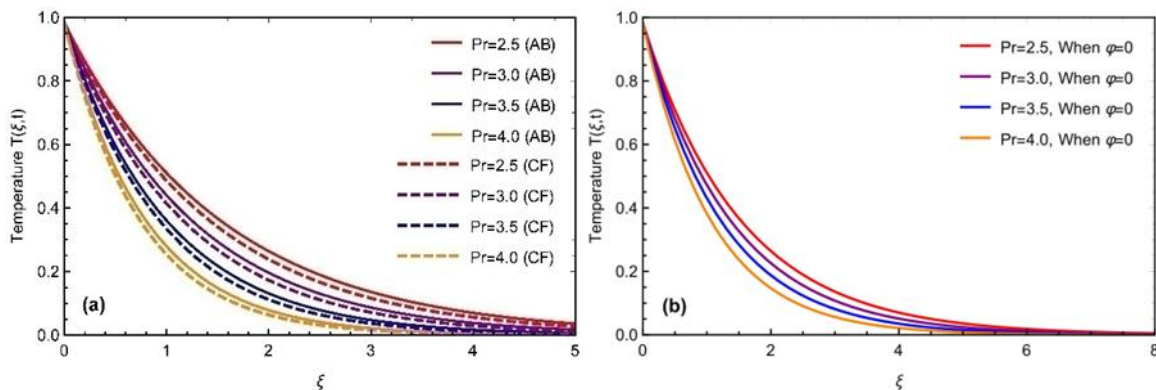


**Figure 4.** Temperature profile against $\xi$ due to $Pr$ when $\alpha, \beta = 0.5, \varphi = 0.0$, and $t = 1.0$.

The effects of the fractional parameters $(\alpha, \beta)$ on velocity are exposed in Figure 5(a) and 5(b). It is noted that the velocity behavior also lessened with growing estimations of the fractional parameters for both cases of fractional approaches. The AB-fractional operators had a more significant impact than CF fractional operators owing to the different kernels of the diverse fractional derivatives on the velocity profile. Figure 5(b) also illustrates the comparison of two different nanoparticles, and we concluded that titanium dioxide $(TiO_2)$-based NFs has a relatively progressive value than copper $(Cu)$-based nanofluid, due to the physical characteristics of the considered nanoparticles, like the thermal profile.
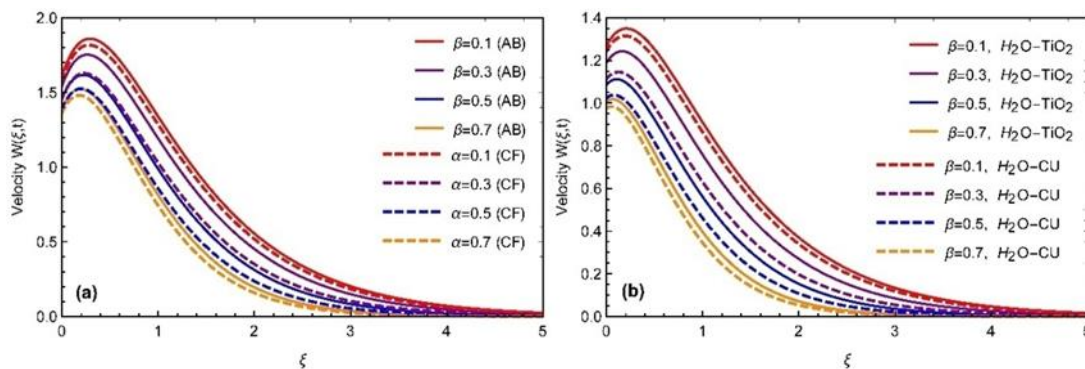


**Figure 5.** Velocity profile against $\xi$ due to $\alpha, \beta$ when $Pr = 6.2$, $Gr = 2.6$, $M = 0.85$, $\theta_1 = \theta_2 = \frac{\pi}{4}$, $K = 2.5$, $h = 0.5$, and $t = 1.0$.

Figure 6(a) and 6(b) were sketched for the profile of the velocity to see the impact of $Pr$ and it is noted that the velocity profile also had reciprocal performance for heat transmission over the whole domain due to the fact that $Pr$ states the ratio of momentum diffusivity to thermal diffusivity. In heat transference models, $Pr$ controls the relative viscosity of the momentum and thermal boundary layers. Figure 6(b) describes the velocity for the normal working-based fluid. The results reveal that, with the rising value of $Pr$, the velocity profile declines. The effects of the volume fraction ($\varphi$) on the velocity are shown in Figure 7(a) and 7(b) for both fractional models. It was detected that the velocity decelerates by increasing the estimations of $\varphi$ because of the thermal conductivity of NFs for the $\varphi$ parameters. Moreover, Figure 7(b) depicts that $TiO_2$-based NFs have a superior velocity value compared to $Cu$-based NFs. Figure 8(a) is portrayed to examine the behavior of $\beta$ on a velocity, along with the slip and no-slip conditions. It is observed that the velocity declines due to more significant estimations of $\beta$. Moreover, it is distinguished that the velocity graph with slip conditions was higher than the graph without slip conditions near the oscillating plate. The effect of the Casson parameter $\lambda_1$ on the velocity is shown in Figure 8(b). It can be seen that the velocity behavior represents the dual behavior for the Casson parameter $\lambda_1$ for both cases of fractional approaches. Initially, the momentum profile decreases due to increase in $\lambda_1$, but and then decelerate its impact and the fluid flows more significantly. The AB-fractional operators have a more significant impact than the CF-fractional operators owing to the different kernels of the diverse fractional derivatives on the velocity.
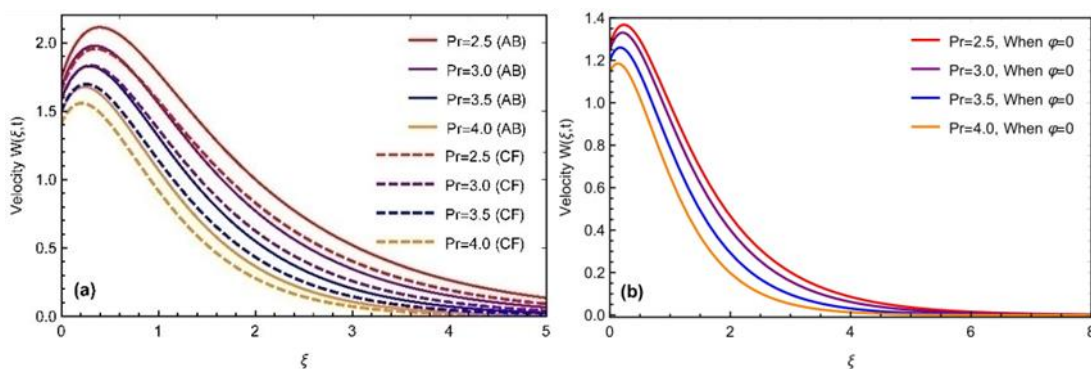


**Figure 6.** Velocity profile against $\xi$ due to $Pr$ when $\alpha, \beta = 0.5, Gr = 2.6, M = 0.85,$ $\theta_1 = \theta_2 = \frac{\pi}{4}$, $K = 2.5$, $h = 0.5$, $\varphi = 0.0$, and $t = 1.0$.
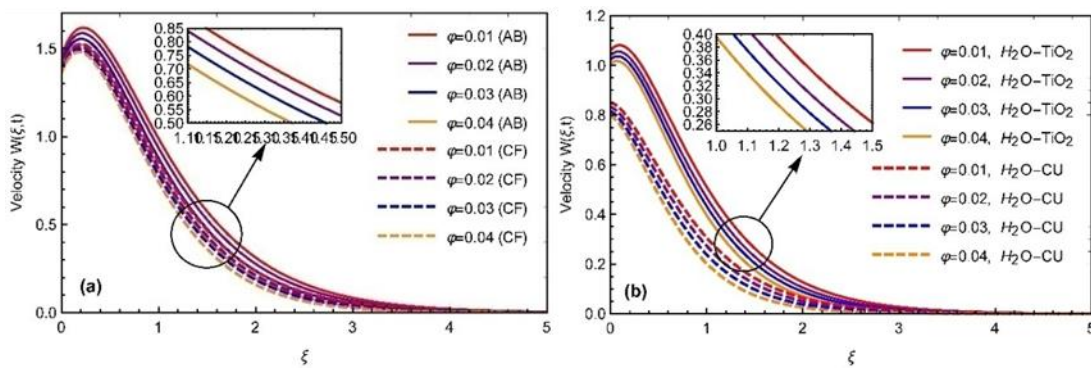


**Figure 7.** Velocity profile against $\xi$ due to $\varphi$ when $\alpha, \beta = 0.5$, $Pr = 6.2, Gr = 2.6,$ $M = 0.85$, $\theta_1 = \theta_2 = \frac{\pi}{4}$, $K = 2.5$, $h = 0.5$, and $t = 1.0$.

**Figure 8.** Velocity profile against $\xi$ due to $h$ when $\alpha, \beta = 0.5$, $Pr = 6.2$, $Gr = 2.6$, $M = 0.85$, $\theta_1 = \theta_2 = \frac{\pi}{4}$, $K = 2.5$, and $t = 1.0$.

Figure 9(a) and 9(b) represent the velocity diagrams that can be used to understand the influence of $Gr$ and $K$, respectively. A rise in the velocity appeared because an enhancement in the estimations of $Gr$ and the decreasing behavior can be seen for the porosity constraint $K$. Physically, the upsurge in the $Gr$ results from significant induced fluid flows because of an increase in buoyancy influences. Consequently, these forces may influence an increase in the velocity. Moreover, for the porosity constraint, physically, when in the porous medium, the holes are significantly sufficient, so the resistance of the permeability medium can be ignored. Therefore, the velocity rises as the existence of the porous surface increases the resistance to the fluid.
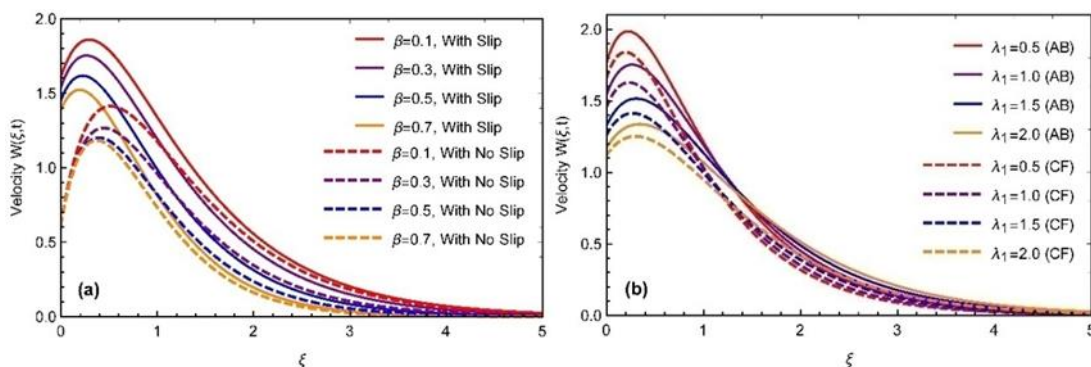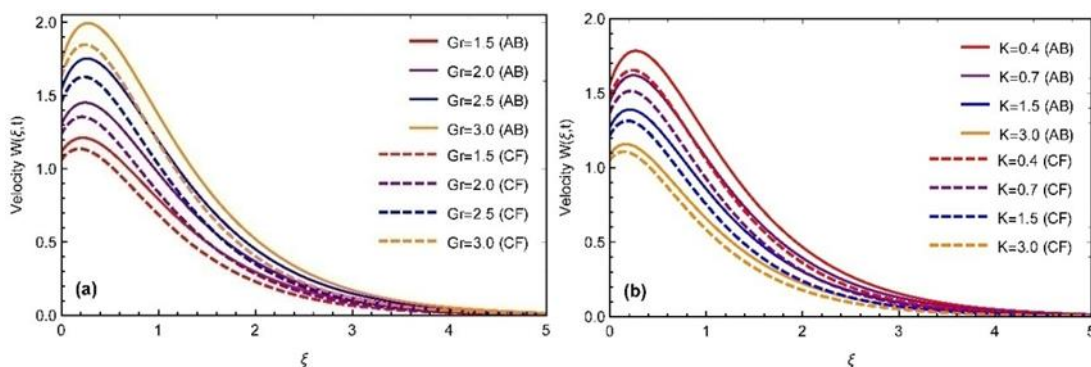


**Figure 9.** Velocity profile against $\xi$ due to $K$ when $\alpha, \beta = 0.5$, $Pr = 6.2$, $Gr = 2.6$, $M = 0.85$, $\theta_1 = \theta_2 = \frac{\pi}{4}$, $h = 0.5$, and $t = 1.0$.

Figure 10(a) illustrates the impact of the magnetic field $M$ on the velocity. It is defined that magnetic field existence creates a Lorentz force in an electrically conducting fluid, which acts inversely to the fluid movement path if the value of $M$ is imposed in the perpendicular direction, decelerating the velocity of the fluid. Furthermore, Figure 10(b) shows a comparison of different nanoparticles, and it is concluded that titanium dioxide ($TiO_2$)-based NFs have a more significant impact on the momentum field as compared to the copper ($Cu$) and aluminum oxide ($Al_2O_3$) nanoparticles. Figure 11(a) and 11(b) signify the effects of ordinary and fractional derivatives on velocity and temperature. It is perceived that the velocity and temperature for the ordinary model were more extensive than those for the AB- and CF-fractional models. Figure 12(a) and 12(b) were drawn to compare two different numerical methods, i.e., the Stehfest and Tzou methods, for thermal and

momentum profiles. The outcomes from both curves show a slight overlap, which signifies this work's validity. Figure 13(a) and 13(b) were plotted to check the validity of our attained results in comparison with the results of Ahmad et al. [25] for velocity and temperature fields, respectively. It can be realized from these figures that our obtained results match those acquired by Ahmad et al. [25] by the overlapping of both curves.
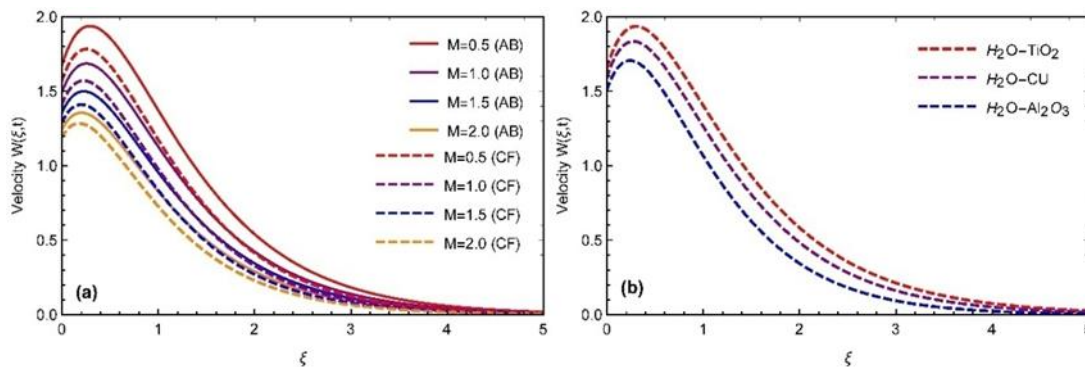


**Figure 10.** Velocity profile against $\xi$ due to $M$ when $\alpha, \beta = 0.5, Pr = 6.2, Gr = 2.6,$ $\theta_1 = \theta_2 = \frac{\pi}{4}, K = 2.5, h = 0.5,$ and $t = 1.0.$
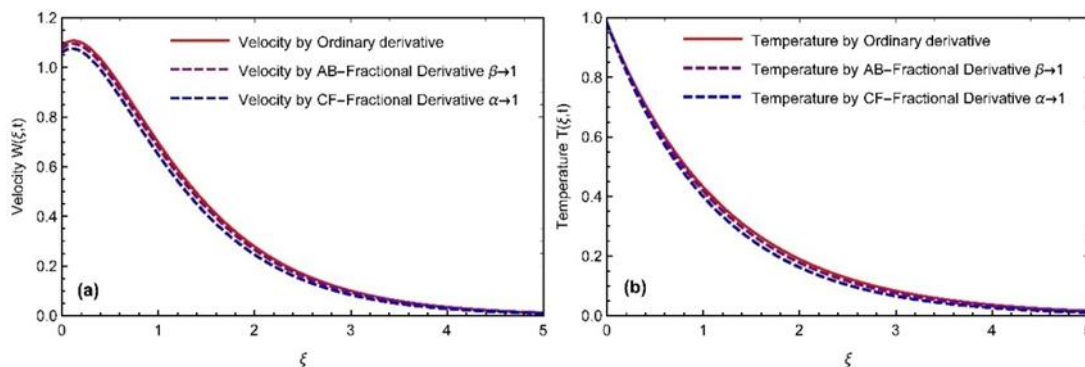


**Figure 11.** Comparison of fractional and ordinary derivative momentum and thermal fields.
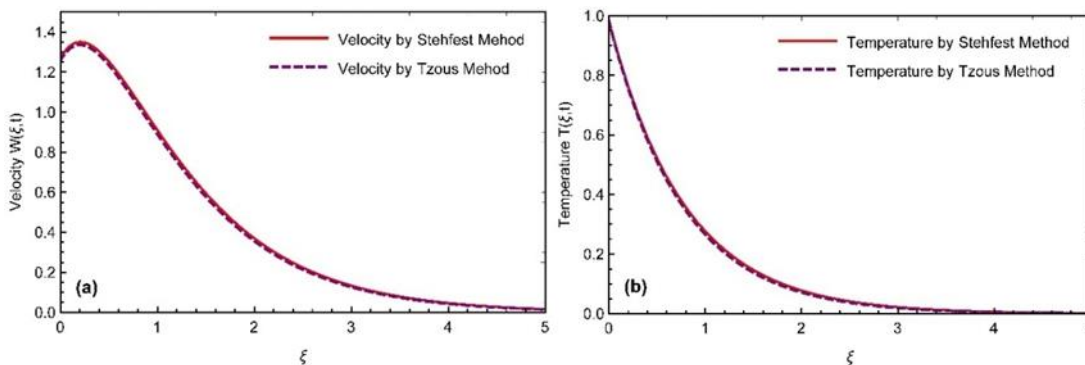


**Figure 12.** Comparison of numerical schemes for momentum and thermal fields.
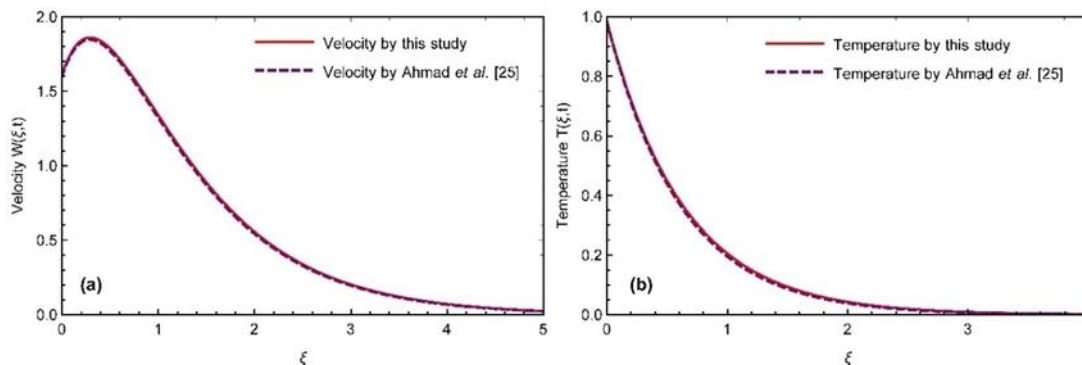
**Figure 13.** Comparison of thermal and momentum profiles with the results of Ahmad et al. [25].

Table 3 shows the numerical analysis of the Nusselt number $Nu$ with the impact of diverse parameters for the AB and CF models. It is perceived that the value of $Nu$ for the CF model is larger than that for the AB model. Physically, it is due to the kernels of different fractional operators. Table 4 signifies the results of the numerical investigation of the skin friction $C_f$ with the disparity in the fractional parameters at various times for the AB- and CF-fractional derivatives; it was concluded that the value of $C_f$ for the CF model was larger than that for the AB model. Table 5 represents the results of the numerical study of velocity and temperature via diverse numerical inverse systems for the validation and accuracy of our obtained results as well as applied techniques. Furthermore, the results of the numerical comparison of our attained temperature and velocity profiles are examined in Table 6.

**Table 3.** Numerical analysis results for the Nusselt number $Nu$ for the AB- and CF-fractional models.

| $\alpha, \beta$ | $\varphi$ | $t$ | $Nu(AB)$ | $Nu(CF)$ |
|---|---|---|---|---|
| 0.1 | 0.00 | 0.1 | 0.6300 | 0.6410 |
| 0.4 | 0.01 | 0.1 | 0.7200 | 0.7589 |
| 0.7 | 0.02 | 0.1 | 0.9153 | 0.9761 |
| 0.9 | 0.03 | 0.1 | 1.2046 | 1.2565 |
| 0.1 | 0.00 | 0.3 | 0.6202 | 0.6310 |
| 0.4 | 0.01 | 0.3 | 0.7088 | 0.7471 |
| 0.7 | 0.02 | 0.3 | 0.9011 | 0.9609 |
| 0.9 | 0.03 | 0.3 | 1.1859 | 1.2369 |
| 0.1 | 0.00 | 0.5 | 0.5955 | 0.6059 |
| 0.4 | 0.01 | 0.5 | 0.6806 | 0.7174 |
| 0.7 | 0.02 | 0.5 | 0.8653 | 0.9227 |
| 0.9 | 0.03 | 0.5 | 1.1387 | 1.1877 |
| 0.1 | 0.00 | 0.8 | 0.6106 | 0.6213 |
| 0.4 | 0.01 | 0.8 | 0.6978 | 0.7356 |
| 0.7 | 0.02 | 0.8 | 0.8872 | 0.9461 |
| 0.9 | 0.03 | 0.8 | 1.1676 | 1.2178 |

**Table 4.** Numerical analysis results for the skin friction $C_f$ at different time.

| $\beta$ | $t = 1.0$ | | $t = 1.5$ | |
|---|---|---|---|---|
| | $C_f\,(AB)$ | $C_f\,(CF)$ | $C_f\,(AB)$ | $C_f\,(CF)$ |
| 0.1 | 0.1201 | 0.1546 | 0.7407 | 0.7590 |
| 0.2 | 0.1384 | 0.1993 | 0.7541 | 0.7851 |
| 0.3 | 0.1679 | 0.2484 | 0.7750 | 0.8150 |
| 0.4 | 0.2083 | 0.3025 | 0.8034 | 0.8496 |
| 0.5 | 0.2601 | 0.3624 | 0.8401 | 0.8903 |
| 0.6 | 0.3243 | 0.4286 | 0.8869 | 0.9391 |
| 0.7 | 0.4027 | 0.5014 | 0.9471 | 0.9990 |
| 0.8 | 0.4967 | 0.5793 | 1.0264 | 1.0747 |
| 0.9 | 0.6050 | 0.6550 | 1.1349 | 1.1720 |

**Table 5.** Numerical analysis results for the velocity and temperature profile.

| $\xi$ | Velocity (Stehfest) | | Velocity (Tzou's) | | Temperature (Stehfest) | | Temperature (Tzou) | |
|---|---|---|---|---|---|---|---|---|
| | AB | CF | AB | CF | AB | CF | AB | CF |
| 0.1 | 1.8385 | 1.8236 | 1.8203 | 1.8179 | 0.7294 | 0.7258 | 0.7389 | 0.7352 |
| 0.3 | 1.9869 | 2.0373 | 1.9890 | 2.0235 | 0.6074 | 0.5984 | 0.6154 | 0.6064 |
| 0.5 | 1.9289 | 2.0150 | 1.9456 | 1.9963 | 0.5059 | 0.4934 | 0.5126 | 0.5000 |
| 0.7 | 1.7664 | 1.8673 | 1.7927 | 1.8461 | 0.4212 | 0.4067 | 0.4269 | 0.4123 |
| 0.9 | 1.5601 | 1.6622 | 1.5917 | 1.6404 | 0.3507 | 0.3353 | 0.3555 | 0.3399 |
| 1.1 | 1.3447 | 1.4401 | 1.3787 | 1.4189 | 0.2920 | 0.2763 | 0.2960 | 0.2802 |
| 1.3 | 1.1394 | 1.2239 | 1.1735 | 1.2041 | 0.2431 | 0.2277 | 0.2464 | 0.2310 |
| 1.5 | 1.9533 | 1.0254 | 0.9862 | 1.0073 | 0.2024 | 0.1876 | 0.2052 | 0.1904 |
| 1.7 | 0.7902 | 0.8498 | 0.8208 | 0.8337 | 0.1684 | 0.1546 | 0.1708 | 0.1569 |
| 1.9 | 0.6502 | 0.6983 | 0.6781 | 0.6842 | 0.1402 | 0.1274 | 0.1422 | 0.1293 |

**Table 6.** Numerical comparison results for the temperature and velocity with Ahmad et al. [25].

| $\xi$ | Temperature by this study | Temperature by Ahmad et al. [25] | Velocity by this study | Velocity by Ahmad et al. [25] |
|---|---|---|---|---|
| 0.1 | 0.9311 | 0.9376 | 0.9407 | 0.9363 |
| 0.3 | 0.7991 | 0.8198 | 0.8710 | 0.8599 |
| 0.5 | 0.6854 | 0.7151 | 0.7658 | 0.7448 |
| 0.7 | 0.5877 | 0.6226 | 0.6516 | 0.6223 |

*Continued on next page*

| $\xi$ | Temperature by this study | Temperature by Ahmad et al. [25] | Velocity by this study | Velocity by Ahmad et al. [25] |
|-----|-----|-----|-----|-----|
| 0.9 | 0.5037 | 0.5412 | 0.5424 | 0.5076 |
| 1.1 | 0.4311 | 0.4696 | 0.4446 | 0.4071 |
| 1.3 | 0.3696 | 0.4068 | 0.3602 | 0.3226 |
| 1.5 | 0.3164 | 0.3520 | 0.2894 | 0.2533 |
| 1.7 | 0.2708 | 0.3041 | 0.2310 | 0.1976 |
| 1.9 | 0.2317 | 0.2624 | 0.1835 | 0.1533 |

## 7. Conclusions

The Casson nanoparticles flow via AB and CF time-fractional derivatives has been studied. An NF mixed with various nanoparticles was assumed with water as the base fluid for the energy and momentum equations. The inversion algorithms as well as the Laplace transform were employed to obtain the solutions of velocity and temperature. A comparison was carried out for the ordinary, AB- and CF models. Some consequences from the literature can also be recovered from our obtained outcomes. Some concluding remarks are as follows:

- Temperature and momentum fields illustrate decaying behavior for fractional parameters in the case of the AB and CF models.
- The response of temperature and velocity fields declined to improve the volume fraction ($\varphi$) for both fractional models.
- The computations show that temperature, as well as the velocity field rate declined by growing $Pr$ for both fractional techniques.
- The velocity behavior also lessened with $\lambda_1$ for both cases of fractional approaches.
- An increasing behavior for the velocity appeared due to an enhancement in the estimations of $Gr$ and decreasing behavior was seen for $K$.
- The behavior of velocity declined with the growing estimations of $M$.
- The velocity and temperature for the ordinary model were more extensive than those for the AB- and CF- fractional models.
- The comparison of the two different numerical methods, i.e., the Stehfest and Tzou methods for thermal and momentum profiles, showed that the outcomes from both curves have a slight overlap.
- Our obtained temperature and velocity profile results match those acquired by Ahmad et al. [25].
- Velocity field increases are more significant than increase in the values of $Gr$.
- The solution attained via the CF approach showed more decaying behavior then the AB model.

## Conflict of interest

The authors declare no conflict of interest.

# References

1. A. Saeedi, M. Akbari, D. Toghraie, An experimental study on rheological behavior of a nanofluid containing oxide nanoparticle and proposing a new correlation, *Physica E*, **99** (2018), 285–293. http://dx.doi.org/10.1016/j.physe.2018.02.018

2. D. Toghraie, N. Sina, M. Mozafarifard, A. Alizadeh, F. Soltani, M. Fazilati, Prediction of dynamic viscosity of a new non-Newtonian hybrid nanofluid using experimental and artificial neural network (ANN) methods, *Heat. Transf. Res.*, **51** (2020), 1351–1362. http://dx.doi.org/10.1615/HeatTransRes.2020034645

3. Y. Zheng, H. Yang, M. Fazilati, D. Toghraie, H. Rahimi, M. Afrand, Experimental investigation of heat and moisture transfer performance of $CaCl_2/H_2O\text{-}SiO_2$ nanofluid in a gas-liquid micro porous hollow fiber membrane contactor, *Int. Commun. Heat Mass*, **113** (2020), 104533. http://dx.doi.org/10.1016/j.icheatmasstransfer.2020.104533

4. D. Yılmaz Aydın, M. Gürü, Nanofluids: preparation, stability, properties, and thermal performance in terms of thermo-hydraulic, thermodynamics and thermo-economic analysis, *J. Therm. Anal. Calorim.*, **147** (2022), 7631–7664. http://dx.doi.org/10.1007/s10973-021-11092-8

5. M. Sanches, A. Moita, A. Ribeiro, A. Moreira, Heat transfer in nanofluid spray cooling of a solid heated surface for cooling systems in civil and military applications, *ICLASS*, **1** (2021), 275. http://dx.doi.org/10.2218/iclass.2021.6000

6. N. Saleem, S. Munawar, Significance of synthetic cilia and Arrhenius energy on double diffusive stream of radiated hybrid nanofluid in microfluidic pump under ohmic heating: An entropic analysis, *Coatings*, **11** (2021), 1292. http://dx.doi.org/10.3390/coatings11111292

7. S. Salman, A. Talib, S. Saadon, M. Hameed Sultan, Hybrid nanofluid flow and heat transfer over backward and forward steps: a review, *Powder Technology*, **363** (2020), 448–472. http://dx.doi.org/10.1016/j.powtec.2019.12.038

8. A. Dalkılıç, Ö. Acikgöz, B. Kücükyildirim, A. Eker, B. Lüleci, C. Jumpholkul, et al., Experimental investigation on the viscosity characteristics of water based $SiO_2$-graphite hybrid nanofluids, *Int. Commun. Heat Mass*, **97** (2018), 30–38. http://dx.doi.org/10.1016/j.icheatmasstransfer.2018.07.007

9. N. Wahid, N. Ariffin, N. Khashi'ie, R. Yahaya, I. Pop, N. Bachok, et al., Three-dimensional radiative flow of hybrid nanofluid past a shrinking plate with suction, *Journal of Advanced Research in Fluid Mechanics and Thermal Sciences*, **85** (2021), 54–70. http://dx.doi.org/10.37934/arfmts.85.1.5470

10. N. Faizal, N. Ariffin, Y. Rahim, M. Hafidzuddin, N. Wahi, MHD and slip effect in micropolar hybrid nanofluid and heat transfer over a stretching sheet with thermal radiation and non-uniform heat source/sink, *CFD Letters*, **12** (2020), 121–130. http://dx.doi.org/10.37934/cfdl.12.11.121130

11. R. Dash, K. Mehta, G. Jayaraman, Casson fluid flow in a pipe filled with a homogeneous porous medium, *Int. J. Eng. Sci.*, **34** (1996), 1145–1156. http://dx.doi.org/10.1016/0020-7225(96)00012-2

12. N. Casson, A flow equation for pigment-oil suspensions of the printing ink type, In: *Rheology of disperse systems*, Oxford: Pergamon Press, 1959, 84–104.

13. G. Vinogradov, A. Malkin, *Rheology of polymers*, Berlin: Springer, 1980.

14. A. Ali, Z. Bukhari, M. Umar, M. Ismail, Z. Abbas, Cu and Cu-SWCNT nanoparticles' suspension in pulsatile Casson fluid flow via Darcy-Forchheimerporous channel with compliant walls: aprospective model for blood flow in stenosed arteries, *Int. J. Mol. Sci.*, **22** (2021), 6494. http://dx.doi.org/10.3390/ijms22126494

15. M. Shahrim, A. Mohamad, L. Jiann, M. Zakaria, S. Shafie, Z. Ismail, et al., Exact solution of fractional convective Casson fluid through an accelerated plate, *CFD Letters*, **13** (2021), 15–25. http://dx.doi.org/10.37934/cfdl.13.6.1525

16. M. Mustafa, T. Hayat, I. Pop, A. Aziz, Unsteady boundary layer flow of a Casson fluid impulsively started moving flat plate, *Heat Transf.-Asian Re.*, **40** (2011), 563–576. http://dx.doi.org/10.1002/htj.20358

17. S. Mukhopadhyay, P. De, K. Bhattacharyya, G. Layek, Casson fluid flow over an unsteady stretching surface, *Ain Shams Eng. J.*, **4** (2013), 933–938. http://dx.doi.org/10.1016/j.asej.2013.04.004

18. A. Khalid, I. Khan, A. Khan, S. Shafie, Unsteady MHD free convection flow of Casson fluid past over an oscillating vertical plate embedded in a porous medium, *Eng. Sci. Technol.*, **18** (2015), 309–317. http://dx.doi.org/10.1016/j.jestch.2014.12.006

19. I. Animasaun, E. Adebile, A. Fagbade, Casson fluid flow with variable thermo-physical property along exponentially stretching sheet with suction and exponentially decaying internal heat generation using the homotopy analysis method, *Journal of the Nigerian Mathematical Society*, **35** (2016), 1–17. http://dx.doi.org/10.1016/j.jnnms.2015.02.001

20. A. Rashad, A. Chamkha, S. El-Kabeir, Effect of chemical reaction on heat and mass transfer by mixed convection flow about a sphere in a saturated porous media, *Int. J. Numer. Method. H.*, **21** (2011), 418–433. http://dx.doi.org/10.1108/09615531111123092

21. O. Makinde, N. Sandeep, T. Ajayi, I. Animasaun, Numerical exploration of heat transfer and Lorentz force effects on the flow of MHD Casson fluid over an upper horizontal surface of a thermally stratified melting surface of a paraboloid of revolution, *Int. J. Nonlin. Sci. Num.*, **19** (2018), 93–106. http://dx.doi.org/10.1515/ijnsns-2016-0087

22. N. Khashi'ie, N. Md Arifin, I. Pop, R. Nazar, Melting heat transfer in hybrid nanofluid flow along a moving surface, *J. Therm. Anal. Calori.*, **147** (2022), 567–578. http://dx.doi.org/10.1007/s10973-020-10238-4

23. N. Khashi'ie, I. Waini, N. Zainal, K. Hamzah, A. Mohd Kasim, Hybrid nanofluid flow past a shrinking cylinder with prescribed surface heat flux, *Symmetry*, **12** (2020), 1493. http://dx.doi.org/10.3390/sym12091493

24. N. Khashi'ie, M. Hafidzuddin, N. Arifin, N. Wahi, Stagnation point flow of hybrid nanofluid over a permeable vertical stretching/shrinking cylinder with thermal stratification effect, *CFD Letters*, **12** (2020), 80–94.

25. M. Ahmad, M. Asjad, A. Akgül, D. Baleanu, Analytical solutions for free convection flow of Casson nanofluid over an infinite vertical plate, *AIMS Mathematics*, **6** (2021), 2344–2358. http://dx.doi.org/10.3934/math.2021142

26. T. Thumma, A. Wakif, I. Animasaun, Generalized differential quadrature analysis of unsteady three-dimensional MHD radiating dissipative Casson fluid conveying tiny particles, *Heat Transf.*, **49** (2020), 2595–2626. http://dx.doi.org/10.1002/htj.21736

27. F. Alwawi, H. Alkasasbeh, A. Rashad, R. Idris, Heat transfer analysis of ethylene glycol-based Casson nanofluid around a horizontal circular cylinder with MHD effect, *P. I. Mech. Eng. C-J. Mec.*, **234** (2020), 2569–2580. http://dx.doi.org/10.1177/0954406220908624

28. F. Alwawi, H. Alkasasbeh, A. Rashad, R. Idris, Natural convection flow of Sodium Alginate based Casson nanofluid about a solid sphere in the presence of a magnetic field with constant surface heat flux, *J. Phys.: Conf. Ser.*, **1366** (2019), 012005. http://dx.doi.org/10.1088/1742-6596/1366/1/012005

29. Q. Ali, S. Riaz, A. Awan, K. Abro, A mathematical model for thermography on viscous fluid based on damped thermal flux, *Z. Naturforsch. A*, **76** (2021), 285–294. http://dx.doi.org/10.1515/zna-2020-0322

30. A. Raza, S. Khan, M. Khan, E. El-Zahar, Heat transfer analysis for oscillating flow of magnetized fluid by using the modified Prabhakar-like fractional derivatives, submitted for publication. http://dx.doi.org/10.21203/rs.3.rs-1086428/v1

31. A. Raza, S. Khan, S. Farid, M. Khan, M. Khan, A. Haq, et al., Transport properties of mixed convective nano-material flow considering the generalized Fourier law and a vertical surface: concept of Caputo-time fractional derivative, *P. I. Mech. Eng. C-J. Mec.*, **236** (2022), 974–984. http://dx.doi.org/10.1177/09576509221075110

32. S. Riaz, M. Sattar, K. Abro, Q. Ali, Thermo-dynamical investigation of constitutive equation for rate type fluid: a semi-analytical approach, *International Journal of Modelling and Simulation*, in press. http://dx.doi.org/10.1080/02286203.2022.2056427

33. A. Awan, S. Riaz, K. Abro, A. Siddiqa, Q. Ali, The role of relaxation and retardation phenomenon of Oldroyd-B fluid flow through Stehfest's and Tzou's algorithms, *Nonlinear Engineering*, **11** (2022), 35–46. http://dx.doi.org/10.1515/nleng-2022-0006

34. Y. Wang, A. Raza, S. Khan, M. Khan, M. Ayadi, M. El-Shorbagy, et al., Prabhakar fractional simulations for hybrid nanofluid with aluminum oxide, titanium oxide and copper nanoparticles along with blood base fluid, *Wave. Random Complex*, in press. http://dx.doi.org/10.1080/17455030.2022.2063983

35. Z. Jie, M. Khan, K. Al-Khaled, E. El-Zahar, N. Acharya, A. Raza, et al., Thermal transport model for Brinkman type nanofluid containing carbon nanotubes with sinusoidal oscillations conditions: a fractional derivative concept, *Wave. Random Complex*, in press. http://dx.doi.org/10.1080/17455030.2022.2049926

36. S. Suganya, M. Muthtamilselvan, Z. Alhussain, Activation energy and Coriolis force on Cu-TiO$_2$/water hybrid nanofluid flow in an existence of nonlinear radiation, *Appl. Nanosci.*, **11** (2021), 933–949. http://dx.doi.org/10.1007/s13204-020-01647-w

37. S. Abu Bakar, N. Md Arifin, N. Khashi'ie, N. Bachok, Hybrid nanofluid flow over a permeable shrinking sheet embedded in a porous medium with radiation and slip impacts, *Mathematics*, **9** (2021), 878. http://dx.doi.org/10.3390/math9080878

38. S. Shoeibi, H. Kargarsharifabad, N. Rahbar, G. Ahmadi, M.Safaei, Performance evaluation of a solar still using hybrid nanofluid glass cooling-CFD simulation and environmental analysis, *Sustain. Energy Techn.*, **49** (2022), 101728. http://dx.doi.org/10.1016/j.seta.2021.101728

39. P. Kanti, K. Sharma, Z. Said, M. Jamei, K.Yashawantha, Experimental investigation on thermal conductivity of fly ash nanofluid and fly ash-Cu hybrid nanofluid: prediction and optimization via ANN and MGGP model, *Particul. Sci. Technol.*, **40** (2022), 182–195. http://dx.doi.org/10.1080/02726351.2021.1929610

40. M. Nadeem, I. Siddique, J. Awrejcewicz, M. Bilal, Numerical analysis of a second-grade fuzzy hybrid nanofluid flow and heat transfer over a permeable stretching/shrinking sheet, *Sci. Rep.*, **12** (2022), 1631. http://dx.doi.org/10.1038/s41598-022-05393-7

41. L. Karthik, G. Kumar, T. Keswani, A. Bhattacharyya, S. Sarath Chandar, K. Bhaskara Rao, Protease inhibitors from marine actinobacteria as a potential source for antimalarial compound, *PloS ONE*, **9** (2014), 90972. http://dx.doi.org/10.1371/journal.pone.0090972

42. N. Shah, I. Khan, Heat transfer analysis in a second grade fluid over and oscillating vertical plate using fractional Caputo-Fabrizio derivatives, *Eur. Phys. J. C*, **76** (2016), 362. http://dx.doi.org/10.1140/epjc/s10052-016-4209-3

43. S. Mondal, N. Haroun, P. Sibanda, The effects of thermal radiation on an unsteady MHD axisymmetric stagnation-point flow over a shrinking sheet in presence of temperature dependent thermal conductivity with Navier slip, *PLoS ONE*, **10** (2015), 0138355. http://dx.doi.org/10.1371/journal.pone.0138355

44. S. Aman, I. Khan, Z. Ismail, M. Salleh, Applications of fractional derivatives to nanofluids: exact and numerical solutions, *Math. Model. Nat. Phenom.*, **13** (2018), 2. http://dx.doi.org/10.1051/mmnp/2018013

45. P. Sreedevi, P. Sudarsana Reddy, M. Sheremet, A comparative study of $Al_2O_3$ and $TiO_2$ nanofluid flow over a wedge with non-linear thermal radiation, *Int. J. Numer. Method. H.*, **30** (2020), 1291–1317. http://dx.doi.org/10.1108/HFF-05-2019-0434

46. A. Atangana, D. Baleanu, New fractional derivatives with nonlocal and non-singular kernel: theory and application to heat transfer model, *Therm. Sci.*, **20** (2016), 763–769. http://dx.doi.org/10.2298/TSCI160111018A

47. M. Riaz, A. Atangana, N. Iftikhar, Heat and mass transfer in Maxwell fluid in view of local and non-local differential operators, *J. Therm. Anal. Calorim.*, **143** (2021), 4313–4329. http://dx.doi.org/10.1007/s10973-020-09383-7

48. M. Caputo, M. Fabrizio, A new definition of fractional derivative without singular kernel, *Progr. Fract. Differ. Appl.*, **1** (2015), 73–85. http://dx.doi.org/10.12785/pfda/010201

49. A. Atangana, On the new fractional derivative and application to nonlinear Fisher's reaction-diffusion equation, *Appl. Math. Comput.*, **273** (2016), 948–956. http://dx.doi.org/10.1016/j.amc.2015.10.021

50. M. Abdullah, A. Butt, N. Raza, E. Haque, Semi-analytical technique for the solution of fractional Maxwell fluid, *Can. J. Phys.*, **95** (2017), 472–478. http://dx.doi.org/10.1139/cjp-2016-0817

51. M. Khan, Z. Hammouch, D. Baleanu, Modeling the dynamics of hepatitis E via the Caputo-Fabrizio derivative, *Math. Model. Nat. Phenom.*, **14** (2019), 311. http://dx.doi.org/10.1051/mmnp/2018074

52. V. Rajesh, Chemical reaction and radiation effects on the transient MHD free convection flow of dissipative fluid past an infinite vertical porous plate with ramped wall temperature, *Chem. Ind. Chem. Eng. Q.*, **17** (2011), 189–198. http://dx.doi.org/10.2298/CICEQ100829003R